

CGM-JEPA: Learning Consistent Continuous Glucose Monitor Representations via Predictive Self-Supervised Pretraining

Hada Melino Muhammad^{1*}, Zechen Li^{1,2,*}, Flora Salim^{1,†}, Ahmed A. Metwally^{2,†}

¹University of New South Wales, ²Google Research, *Equal Contribution: hada_melino.muhammad@unsw.edu.au, zechenl@google.com, [†]Correspondence: aametwally@google.com, flora.salim@unsw.edu.au

Continuous Glucose Monitoring (CGM) shows promise for detecting early metabolic subphenotypes such as insulin resistance (IR) and β -cell dysfunction, but its deployment for population-scale metabolic stratification faces two coupled problems. First, the same physiological state appears through multiple representational forms (raw CGM time series, sparse venous OGTT, distributional summaries such as Glucodensity), so a representation tied to a single view fails to transfer when deployment shifts the modality or setting. Second, baselines evaluated under such shifts perform inconsistently: each ranks well in some regimes and poorly in others. Both problems point to one remedy: representations that abstract away from any single view to capture higher-level temporal and distributional structure. We propose CGM-JEPA, a self-supervised predictive pretraining framework which predicts masked latent representations rather than reconstructing raw values, yielding abstraction that transfers across modalities. X-CGM-JEPA adds a masked Glucodensity cross-view objective that contributes complementary information from a distributional view. We pretrain on $\sim 389k$ unlabeled CGM readings from 228 subjects and evaluate on two clinical cohorts (Initial: $N = 27$; Validation: $N = 17$ in the public-release subset) across cohort generalization, venous-to-CGM transfer, and home CGM regimes, under a 20-iteration \times 2-fold cross-validation protocol. X-CGM-JEPA ranks first or second on AUROC for both endpoints across all three evaluation regimes while no baseline stays in the top three, exceeding the strongest baseline by up to +6.5 AUROC points in cohort generalization and +3.6 points in venous-to-CGM transfer (paired Wilcoxon, $p < 0.001$). The cross-view design pays off where it should: in deployment settings under modality shift, X-CGM-JEPA matches mean AUROC while redistributing performance toward weaker subgroups (ethnicity AUROC gap shrinks 25–54% under transfer); in the in-domain venous setting, where temporal context is sparse, the Glucodensity view lifts label-aware clustering (ARI +39%, NMI +40% on the Initial cohort). Code, de-identified consented data, and pretrained weights are available at <https://github.com/cruiseresearchgroup/CGM-JEPA>.

1. Introduction

Continuous glucose monitoring (CGM) enables dense, continuous measurements of glucose dynamics and is increasingly adopted in normoglycemic and prediabetic populations [11, 25, 26]. Beyond tracking average glucose levels, a central clinical goal is to uncover *latent metabolic dysfunctions* that may underlie superficially similar glucose trajectories. In particular, insulin resistance and β -cell dysfunction represent two distinct physiological mechanisms on the path toward Type 2 Diabetes, yet they can produce overlapping CGM patterns depending on diet, activity, and daily routines. Accurately distinguishing these dysfunctions from CGM would enable earlier risk stratification and personalized intervention.

Despite this promise, deploying CGM-based subphenotype prediction at population scale faces two coupled problems. The first is a *multi-view representation problem*: the same physiological state

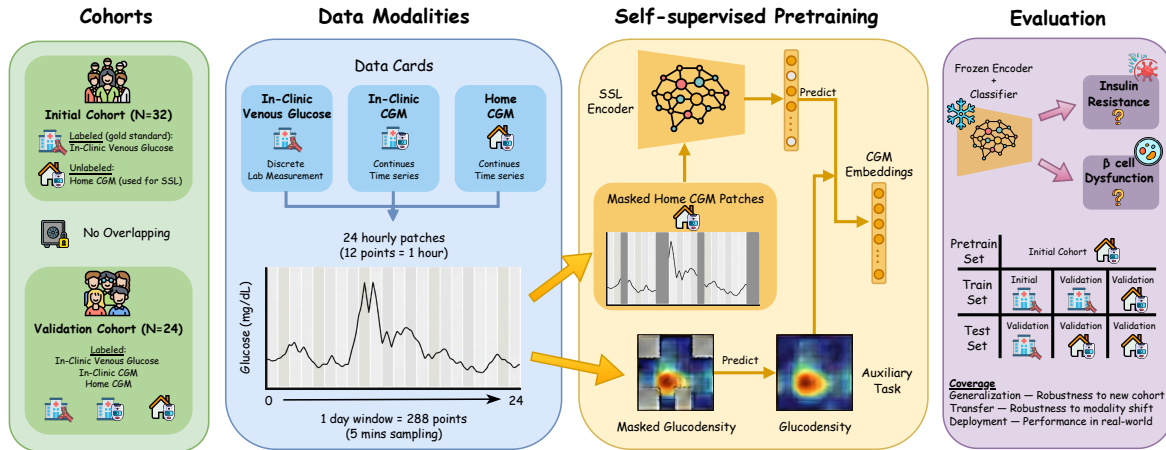


Figure 1 | Study overview. Two cohorts with venous (gold-standard) and CGM measurements from controlled (In-Clinic) and free-living (Home) settings. We pretrain on unlabeled Home CGM (Initial cohort plus the public Colás cohort, with validation subjects excluded), then evaluate metabolic dysfunction prediction under cohort generalization, venous-to-CGM transfer, and home CGM settings.

appears through multiple representational forms, including raw CGM time series, sparse venous OGTT measurements, and distributional summaries such as Glucodensity. Each view captures different aspects of glucose physiology, and a representation tied to any single view tends to fail when deployment shifts the modality (venous to CGM), the setting (controlled to free-living), or the cohort. The second is a *consistency problem*: methods evaluated under such shifts perform inconsistently, with each baseline ranking well in some regimes and poorly in others, leaving no reliable choice for end-to-end CGM deployment. Together, these problems mean that label scarcity (gold-standard venous OGTT labels are costly and invasive [23]) compounds with view fragility, and a method that performs well in one regime offers no guarantee in another.

Both problems point to a single underlying remedy: representations that abstract away from any specific view to capture higher-level temporal and distributional structure that is invariant across modalities and settings. Prior work on CGM modeling [22, 23, 29] often relies on handcrafted feature pipelines (e.g., summary statistics or engineered glycemic indices) that operate on a single view and may not be stable under cohort and setting shifts. Recent time-series foundation models [1, 8, 10, 12, 17, 19, 31] and self-supervised learning approaches [4, 6, 13, 14, 32] reduce reliance on labels, but most are evaluated within a single domain or modality and do not target the clinically realistic regime where supervision and deployment differ in both modality and setting. Many also rely on raw-signal reconstruction or contrastive augmentation objectives, which tie representations to surface signal properties rather than higher-level abstraction. This motivates the question we study: *can we learn CGM representations that abstract beyond any single view and deliver consistent performance across the deployment regimes that matter for population-scale metabolic stratification?*

We address this question using a two-cohort design with complementary modality availability, enabling systematic evaluation across realistic deployment conditions. The *Initial cohort* provides paired venous and home CGM measurements for one set of subjects, while the *Validation cohort* provides labeled venous measurements alongside CGM collected in both controlled and home settings, supporting cross-cohort and cross-modality transfer evaluation. We pretrain representations using unlabeled home CGM from the Initial cohort and the publicly available Colás cohort [7], with all validation-cohort subjects excluded from pretraining to prevent leakage. Figure 1 summarizes the cohorts,

modalities, SSL pretraining pipeline, and downstream tasks. Our evaluation focuses on two binary outcomes (insulin resistance and β -cell dysfunction) under three clinically motivated regimes that span both deployment paths: cohort generalization, venous-to-CGM transfer, and real-world home CGM.

To deliver abstraction-first representations, we adopt a Joint Embedding Predictive Architecture [2, 3, 5, 9, 28]. JEPA’s defining choice is to predict in latent space rather than reconstruct raw values, which encourages the encoder to capture higher-level structure that survives view changes rather than memorizing surface signal properties. We instantiate this as CGM-JEPA, a masked representation prediction objective for 1-day CGM windows that predicts latent representations of masked temporal patches [24] from the visible context. Building on this, X-CGM-JEPA extends the abstraction principle from a single view to multiple views: it adds an auxiliary predictive objective that predicts masked Glucodensity representations from the CGM context embedding, deliberately injecting complementary high-level information from a distributional view of the same window. Conceptually, X-CGM-JEPA treats abstraction as *additive*: when one view leaves gaps, the complementary view fills them; when both views agree, they reinforce each other.

Across a broad set of baselines, including classical unsupervised projection [27, 30], CGM-specific foundation models [20], and modern time-series foundation models [10, 12], the CGM-JEPA family delivers the consistency baselines lack. X-CGM-JEPA ranks first or second on AUROC for both endpoints (IR and β -cell dysfunction) across all three evaluation regimes (in-domain venous, in-domain home CGM, and venous-to-CGM transfer), while no baseline stays in the top three throughout, with each strong baseline winning some regimes and losing others. The cross-view design then pays off in two distinct regimes that map directly to the additive-abstraction principle. In deployment settings under modality shift, X-CGM-JEPA matches mean AUROC against CGM-JEPA but redistributes performance toward weaker demographic subgroups, indicating that the additional distributional view stabilizes representations under shift. In the in-domain venous setting, where the temporal context is sparse compared to continuous CGM, the Glucodensity view contributes additive structure that lifts label-aware clustering agreement, supporting the broader claim that complementary high-level information from a different view genuinely augments a temporal-only representation. To our knowledge, this is the first JEPA-style masked representation prediction framework instantiated for CGM time-series. Our contributions are threefold:

- **Deployment-oriented problem formulation and protocol.** We formalize CGM subphenotype prediction as a two-path deployment problem (in-domain home CGM and venous-to-CGM transfer), under multi-view representation pressure and across three clinically motivated regimes evaluated within a unified, variance-controlled protocol (20-iteration \times 2-fold subject-level cross-validation).
- **Abstraction-first CGM self-supervision.** We introduce CGM-JEPA, a JEPA-style masked latent prediction framework that operationalizes representation abstraction for CGM, yielding embeddings that consistently rank in the top two across all evaluation regimes while no baseline does.
- **Additive cross-view abstraction.** We propose X-CGM-JEPA, which extends the abstraction principle by predicting masked Glucodensity latents alongside CGM, contributing complementary high-level information from a distributional view. The cross-view design yields regime-specific value: subgroup-robust performance under deployment shift, and improved label-aware structure when the temporal view is data-thin.

2. Results

We evaluate two binary outcomes (insulin resistance, IR; β -cell dysfunction) under three clinically motivated regimes that span both deployment paths introduced in Section 1: (i) in-domain home

Table 1 | In-Domain Home CGM: β -cell Dysfunction.

Method	AUROC	F1-score	PRAUC
PCA	0.925 \pm 0.069	0.760 \pm 0.122	0.909 \pm 0.081
GLUFORMER	0.857 \pm 0.121	0.649 \pm 0.111	0.809 \pm 0.160
TS2Vec	0.854 \pm 0.140	0.738 \pm 0.118	0.880 \pm 0.107
MOMENT _{Small}	0.849 \pm 0.094	0.591 \pm 0.164	0.834 \pm 0.096
MOMENT _{Large}	0.652 \pm 0.147	0.511 \pm 0.172	0.649 \pm 0.141
Mantis	0.758 \pm 0.098	0.573 \pm 0.175	0.777 \pm 0.089
CGM-JEPA	<u>0.932 \pm 0.077</u>	<u>0.806 \pm 0.166</u>	<u>0.931 \pm 0.076</u>
X-CGM-JEPA	0.946 \pm 0.063	0.811 \pm 0.169	0.941 \pm 0.066

Table 2 | In-Domain Home CGM: Insulin Resistance.

Method	AUROC	F1-score	PRAUC
PCA	0.821 \pm 0.133	0.694 \pm 0.151	0.842 \pm 0.114
GLUFORMER	0.889 \pm 0.103	0.701 \pm 0.105	<u>0.880 \pm 0.114</u>
TS2Vec	0.848 \pm 0.130	0.676 \pm 0.148	<u>0.868 \pm 0.101</u>
MOMENT _{Small}	0.819 \pm 0.101	0.640 \pm 0.148	0.829 \pm 0.089
MOMENT _{Large}	0.605 \pm 0.127	0.537 \pm 0.143	0.651 \pm 0.124
Mantis	0.690 \pm 0.127	0.570 \pm 0.128	0.759 \pm 0.093
CGM-JEPA	0.842 \pm 0.118	<u>0.746 \pm 0.168</u>	0.872 \pm 0.091
X-CGM-JEPA	<u>0.857 \pm 0.112</u>	0.754 \pm 0.161	0.883 \pm 0.086

CGM, (ii) venous-to-CGM transfer, and (iii) in-domain venous (cohort generalization). All methods follow an identical evaluation protocol: subject-level stratified 2-fold cross-validation repeated over 20 random iterations (40 evaluations per cell), with frozen embeddings probed by Logistic Regression. We report mean \pm std AUROC, F1-score, and PRAUC averaged across runs; best and second-best are highlighted in bold and underlined respectively. All X-CGM-JEPA results in this section use the fixed auxiliary weight $\lambda=1$.

Our headline findings are twofold. First, the CGM-JEPA family delivers *consistency* that no baseline matches: across every (endpoint \times regime) cell, X-CGM-JEPA ranks first or second on AUROC, while every baseline drops to rank three or worse in at least one cell. Pooled across 108 paired comparisons (3 metrics \times 6 endpoint-regime cells \times 6 baselines), CGM-JEPA wins 101/108 and X-CGM-JEPA wins 103/108 (paired Wilcoxon, $p < 0.001$ for both). Second, X-CGM-JEPA’s additive cross-view design yields its clearest distinct contribution in two specific regimes that map directly to the abstraction-as-additive principle introduced in Section 1: in deployment under modality shift, where Glucodensity stabilizes performance across demographic subgroups (Section 2.6); and in the in-domain venous setting, where the temporal context is sparse and the distributional view contributes complementary structure that lifts label-aware clustering (Section 2.4).

2.1. In-Domain Home CGM

We first evaluate the deployment-relevant in-domain home CGM regime: training and evaluation both use free-living home CGM within the validation cohort. This regime most closely matches population-scale deployment, where wearable CGM is collected under unconstrained daily-life conditions and exhibits behavioral variability, sensor noise, and missingness that the in-clinic measurements do not.

β -cell Dysfunction. Table 1 shows that X-CGM-JEPA achieves the best AUROC, F1, and PRAUC on β -cell prediction, with CGM-JEPA second across all three metrics. Compared to the strongest baseline (PCA), X-CGM-JEPA improves AUROC by +2.1 pp, F1 by +5.1 pp, and PRAUC by +3.2 pp. The two JEPA variants form a tight pair, with X-CGM-JEPA marginally ahead on AUROC (+0.014) and

Table 3 | Venous \rightarrow Home CGM: β -cell Dysfunction.

Method	AUROC	F1-score	PRAUC
PCA	0.927 \pm 0.074	0.673 \pm 0.103	0.911 \pm 0.088
GLUFORMER	0.801 \pm 0.129	0.634 \pm 0.104	0.756 \pm 0.160
TS2Vec	0.805 \pm 0.131	0.691 \pm 0.144	0.754 \pm 0.167
MOMENT _{Small}	0.736 \pm 0.192	0.609 \pm 0.157	0.751 \pm 0.173
MOMENT _{Large}	0.606 \pm 0.229	0.431 \pm 0.212	0.615 \pm 0.228
Mantis	0.821 \pm 0.102	0.661 \pm 0.154	0.826 \pm 0.105
CGM-JEPA	<u>0.946 \pm 0.063</u>	<u>0.697 \pm 0.094</u>	<u>0.941 \pm 0.066</u>
X-CGM-JEPA	0.949 \pm 0.061	0.702 \pm 0.103	0.943 \pm 0.064

Table 4 | Venous \rightarrow Home CGM: Insulin Resistance.

Method	AUROC	F1-score	PRAUC
PCA	0.827 \pm 0.146	0.659 \pm 0.111	0.847 \pm 0.125
GLUFORMER	0.530 \pm 0.196	0.537 \pm 0.140	0.555 \pm 0.162
TS2Vec	0.713 \pm 0.181	0.588 \pm 0.158	0.720 \pm 0.142
MOMENT _{Small}	0.830 \pm 0.192	0.667 \pm 0.188	0.852 \pm 0.141
MOMENT _{Large}	0.713 \pm 0.216	0.556 \pm 0.233	0.750 \pm 0.180
Mantis	0.766 \pm 0.146	0.649 \pm 0.178	0.809 \pm 0.109
CGM-JEPA	0.866 \pm 0.114	<u>0.671 \pm 0.094</u>	<u>0.892 \pm 0.086</u>
X-CGM-JEPA	<u>0.865 \pm 0.115</u>	0.689 \pm 0.092	0.892 \pm 0.087

PRAUC (+0.010). Two further patterns are notable. First, only the JEPA variants exceed F1 = 0.80 (0.811 and 0.806), while the next best baseline (PCA) reaches 0.760, a 5-point gap that translates directly to operating-point performance for screening deployment. Second, X-CGM-JEPA attains the lowest fold-to-fold AUROC standard deviation among all methods (0.063 vs. PCA 0.069), indicating that the JEPA family’s consistency extends from cross-regime stability to within-regime robustness.

Insulin Resistance. For insulin resistance (Table 2), GLUFORMER achieves the best AUROC (0.889), edging X-CGM-JEPA by 3.2 pp. This is the single endpoint–regime cell where a baseline outranks the JEPA family on AUROC. The advantage is regime-specific: GLUFORMER trails the JEPA family by 7 to 34 AUROC points across the other five endpoint–regime cells, with near-random performance (0.530) on Venous-to-CGM IR transfer (Section 2.2). X-CGM-JEPA stays competitive (0.857, second) and achieves the best F1 (0.754) and PRAUC (0.883), indicating a more favorable threshold-dependent profile despite the AUROC gap. Across both endpoints, the JEPA family stays in the top two; no baseline does.

2.2. Cross-Modality Transfer

We next evaluate the cross-modality deployment path: classifiers are trained on venous-supervised embeddings and tested on home-CGM embeddings within the validation cohort. This regime mirrors a practical screening scenario in which gold-standard labels come from clinical venous assays but inference at scale is performed on consumer-grade wearable CGM, exposing methods to a simultaneous modality shift (venous to CGM) and setting shift (controlled to free-living).

β -cell Dysfunction. Under venous-to-CGM transfer (Table 3), X-CGM-JEPA is best on all three metrics and CGM-JEPA is second, forming a tight pair (X-vanilla Δ AUROC +0.003, Δ F1 +0.005). Compared to the strongest baseline (PCA), X-CGM-JEPA improves AUROC by +2.2 pp, F1 by +1.1 pp, and PRAUC by +3.2 pp. The more informative pattern is variance, not the mean: X-CGM-JEPA attains AUROC std 0.061, against 0.074 for PCA, 0.129 for GLUFORMER, and 0.229 for MOMENT_{Large}.

Table 5 | In-Domain Venous (Cohort Generalization): β -cell Dysfunction.

Method	AUROC	F1-score	PRAUC
PCA	0.790 \pm 0.109	0.618 \pm 0.096	0.784 \pm 0.101
GLUFORMER	0.742 \pm 0.182	0.598 \pm 0.121	0.703 \pm 0.197
TS2Vec	0.735 \pm 0.180	0.555 \pm 0.192	0.716 \pm 0.171
MOMENT _{Small}	0.712 \pm 0.029	0.574 \pm 0.047	0.668 \pm 0.047
MOMENT _{Large}	0.683 \pm 0.055	0.570 \pm 0.061	0.604 \pm 0.091
Mantis	0.674 \pm 0.115	0.560 \pm 0.066	0.634 \pm 0.141
CGM-JEPA	<u>0.845 \pm 0.112</u>	<u>0.645 \pm 0.084</u>	0.821 \pm 0.113
X-CGM-JEPA	0.855 \pm 0.064	0.664 \pm 0.061	<u>0.815 \pm 0.080</u>

Table 6 | In-Domain Venous (Cohort Generalization): Insulin Resistance.

Method	AUROC	F1-score	PRAUC
PCA	0.744 \pm 0.014	0.610 \pm 0.042	0.770 \pm 0.032
GLUFORMER	0.709 \pm 0.054	0.580 \pm 0.053	0.758 \pm 0.064
TS2Vec	0.733 \pm 0.043	0.621 \pm 0.040	0.741 \pm 0.058
MOMENT _{Small}	0.674 \pm 0.049	0.576 \pm 0.055	0.671 \pm 0.075
MOMENT _{Large}	0.630 \pm 0.063	0.611 \pm 0.056	0.579 \pm 0.070
Mantis	0.709 \pm 0.061	0.582 \pm 0.076	0.687 \pm 0.091
CGM-JEPA	0.801 \pm 0.009	<u>0.631 \pm 0.035</u>	0.824 \pm 0.008
X-CGM-JEPA	<u>0.800 \pm 0.014</u>	0.653 \pm 0.046	<u>0.822 \pm 0.020</u>

Transfer is precisely the regime where high-variance behavior would most concern a deployer, and it is here that the JEPA family is most stable.

Insulin Resistance. For IR transfer (Table 4), CGM-JEPA achieves the best AUROC (0.866) and X-CGM-JEPA the best F1 (0.689) and PRAUC (0.892, tied). Against the strongest baseline (MOMENT_{Small} at 0.830), the JEPA family improves AUROC by +3.6 pp, F1 by +2.2 pp, and PRAUC by +4.0 pp. Two baselines collapse under IR transfer: GLUFORMER drops to 0.530 (near-random) and MOMENT_{Large} to 0.713, both with AUROC std above 0.19. The JEPA family holds AUROC std at 0.114–0.115, the lowest among all methods in this cell, indicating that abstraction-first pretraining delivers stable transfer where reconstruction-based and broad time-series baselines do not.

Across both endpoints, transfer is the regime in which the JEPA family’s advantage is largest in absolute terms and most uniform across metrics: X-CGM-JEPA or CGM-JEPA ranks first on every metric in both endpoints, with the cross-view variant contributing consistent F1 gains over CGM-JEPA under modality shift, consistent with the additive cross-view design.

2.3. Cohort Generalization

We finally evaluate the cohort-generalization regime: encoders are pretrained as before, and downstream classifiers are trained on the Initial cohort venous data and tested on the Validation cohort venous data. Unlike the previous two regimes, this is a capability check rather than a deployment scenario, since population-scale screening cannot rely on venous OGTT at inference. The setting is informative for two reasons. First, the venous modality is the gold-standard supervision source, so strong cohort generalization here is necessary for downstream transfer to be meaningful. Second, venous sampling is much sparser than continuous CGM (CGM samples at a 5-minute interval, while venous OGTT yields only a few discrete timepoints per session), making this the regime in which the cross-view design’s promise of additive distributional structure from a complementary view is most directly testable.

Table 7 | Core clustering-based representation metrics. Higher is better for Silhouette (Sil) and Calinski–Harabasz (CH), while lower is better for Davies–Bouldin (DB). *Bold/underline: best/second-best per dataset–modality.*

Initial cohort – Venous			Validation cohort – CGM			Validation cohort – Venous					
Model	Sil \uparrow	CH \uparrow	DB \downarrow	Model	Sil \uparrow	CH \uparrow	DB \downarrow	Model	Sil \uparrow	CH \uparrow	DB \downarrow
PCA	0.1649	9.1153	1.5843	PCA	0.3022	10.1571	1.1455	PCA	0.1818	6.4728	1.3882
GluFormer	0.0652	3.5545	2.9108	GluFormer	0.1073	3.5875	1.8875	GluFormer	0.1022	3.1786	2.1317
TS2Vec	0.0395	2.2737	3.7784	TS2Vec	0.1443	3.5651	1.9525	TS2Vec	0.0875	2.3896	2.4046
Mantis	0.0262	1.7092	3.7788	Mantis	0.0723	2.2533	2.4958	Mantis	0.0520	1.7887	2.8017
MOMENT	0.1013	3.0752	2.6811	MOMENT	0.0826	3.3272	1.8629	MOMENT	0.0423	1.9287	2.6529
CGM-JEPA	<u>0.1859</u>	<u>11.4096</u>	<u>1.4805</u>	CGM-JEPA	0.3756	<u>15.4511</u>	<u>0.9123</u>	CGM-JEPA	0.2220	8.3631	1.2411
X-CGM-JEPA	0.1940	11.8594	1.4610	X-CGM-JEPA	<u>0.3636</u>	15.4819	0.9033	X-CGM-JEPA	<u>0.1991</u>	<u>8.0749</u>	<u>1.2372</u>

β -cell Dysfunction. On the cohort-generalization β -cell task (Table 5), X-CGM-JEPA achieves the best AUROC (0.855) and F1 (0.664), with CGM-JEPA second on both and best on PRAUC. Compared to the strongest baseline (PCA at 0.790), the JEPA family improves AUROC by **+6.5 pp**, F1 by **+4.6 pp**, and PRAUC by **+3.7 pp**, the largest absolute downstream gains in the paper. The cross-view contribution is also most visible in this regime on a metric beyond F1: X-CGM-JEPA reduces AUROC standard deviation from 0.112 (CGM-JEPA) to 0.064, a 43% relative reduction in fold-to-fold variance from the same encoder architecture under the same protocol. This is consistent with the additive cross-view design: when the temporal view is sparse, the distributional view contributes complementary structure that stabilizes the representation across cross-validation splits.

Insulin Resistance. For IR cohort generalization (Table 6), CGM-JEPA and X-CGM-JEPA are tied on AUROC (0.801 vs 0.800) and PRAUC (0.824 vs 0.822), with X-CGM-JEPA clearly ahead on F1 (0.653 vs 0.631, +2.2 pp). Against the strongest baseline (PCA at 0.744), the JEPA family improves AUROC by **+5.7 pp**, F1 by **+3.2 pp** (over TS2Vec), and PRAUC by **+5.4 pp**. As in the previous two regimes, F1 is where X-CGM-JEPA contributes its most consistent gain over CGM-JEPA, accumulating to a within-family pattern of +0.005 (β -cell home), +0.018 (IR transfer), +0.019 (β -cell venous), and +0.022 (IR venous) across the four cells where the cross-view variant is not directly tied or ahead on AUROC.

The cohort-generalization regime delivers the largest AUROC gains in the paper but, equally importantly, it is where the cross-view design’s distinctive contribution becomes quantitatively visible beyond F1: a halving of fold-to-fold variance on β -cell, and the most concentrated F1 gain pattern across the family. We trace these effects to the representation level in Section 2.4, where the additive distributional view leaves its strongest fingerprint on label-aware clustering structure.

2.4. Representation Quality Analysis

To complement downstream classification, we examine the intrinsic geometry of learned embeddings using three families of unsupervised metrics: clustering quality (Silhouette, Calinski–Harabasz, Davies–Bouldin), distance-based structure (Between/Within ratio, Intra/Inter-cluster distance), and label-aware clustering agreement (Adjusted Rand Index, Normalized Mutual Information). The first two characterize how compact and well-separated the embeddings are without reference to outcome labels; the third tests whether the unsupervised cluster structure aligns with the clinical labels themselves. We compute all metrics on representations pooled across both outcomes (insulin resistance and β -cell dysfunction), reported separately by cohort and modality.

Table 8 | Distance-based representation structure metrics. Higher is better for Between/Within (B/W) ratio and Inter-cluster distance, while lower is better for Intra-cluster distance. *Bold/underline: best/second-best per dataset–modality.*

Initial cohort – Venous				Validation cohort – CGM				Validation cohort – Venous			
Model	B/W ↑	Intra ↓	Inter ↑	Model	B/W ↑	Intra ↓	Inter ↑	Model	B/W ↑	Intra ↓	Inter ↑
PCA	0.3717	3.4512	4.5982	PCA	0.7735	3.6451	6.4387	PCA	0.4933	3.9220	5.7331
GluFormer	0.1448	3.1492	2.3278	GluFormer	0.2697	2.4202	2.5665	GluFormer	0.2432	2.9239	2.8285
TS2Vec	0.0925	1.9931	1.1624	TS2Vec	0.2690	1.9297	1.9826	TS2Vec	0.1805	1.9579	1.6346
Mantis	0.0705	23.3958	12.4460	Mantis	0.1706	23.5024	18.9659	Mantis	0.1355	22.8127	16.4026
MOMENT	0.1270	0.6956	0.5161	MOMENT	0.2482	0.6301	0.6869	MOMENT	0.1442	0.6397	0.5125
CGM-JEPA	0.4640	2.8409	4.1533	CGM-JEPA	<u>1.1825</u>	2.6162	5.8530	CGM-JEPA	0.6406	3.0579	5.0624
X-CGM-JEPA	0.4819	2.5221	3.7567	X-CGM-JEPA	1.1845	2.3348	5.2742	X-CGM-JEPA	<u>0.6185</u>	2.7167	4.5175

Table 9 | Label-agreement clustering metrics (KMeans cluster assignments vs. true metabolic labels). Higher is better for both Adjusted Rand Index (ARI) and Normalized Mutual Information (NMI). *Bold/underline: best/second-best per dataset–modality.* Ties between CGM-JEPA, X-CGM-JEPA, and PCA on the validation cohort arise because the 2-cluster KMeans partition happens to coincide across these well-structured embeddings at $n \approx 17$.

Initial cohort – Venous			Validation cohort – CGM			Validation cohort – Venous		
Model	ARI ↑	NMI ↑	Model	ARI ↑	NMI ↑	Model	ARI ↑	NMI ↑
PCA	<u>0.2246</u>	<u>0.2013</u>	PCA	0.4707	0.3853	PCA	0.3091	<u>0.2506</u>
GluFormer	0.1567	0.1414	GluFormer	−0.0441	0.1159	GluFormer	−0.0441	0.1159
TS2Vec	0.1562	0.1421	TS2Vec	0.3088	0.2605	TS2Vec	<u>0.3088</u>	0.2605
Mantis	−0.0262	0.0116	Mantis	0.1765	0.1463	Mantis	0.0736	0.1380
MOMENT	0.0956	0.1671	MOMENT	0.0071	0.2009	MOMENT	−0.0515	0.0352
CGM-JEPA	0.2079	0.1773	CGM-JEPA	0.4707	0.3853	CGM-JEPA	0.3091	<u>0.2506</u>
X-CGM-JEPA	0.2881	0.2486	X-CGM-JEPA	0.4707	0.3853	X-CGM-JEPA	0.3091	<u>0.2506</u>

Clustering and Distance Structure. Tables 7 and 8 show the JEPA family delivers the strongest geometric structure across all three cohort–modality blocks, with no block in which a baseline outranks both CGM-JEPA and X-CGM-JEPA. On the Initial cohort venous block, X-CGM-JEPA is best on every geometric metric (Sil 0.194, CH 11.86, DB 1.46, B/W 0.48), with CGM-JEPA second across all of them. On the Validation cohort CGM block (the deployment-relevant modality), the two variants split the wins: CGM-JEPA attains the best Silhouette while X-CGM-JEPA attains the best CH and DB, and both lift the B/W ratio by over 50% relative to PCA (1.18 vs. 0.77). On the Validation cohort venous block, CGM-JEPA is best on all three clustering metrics and on B/W. The geometric advantage is therefore not specific to any one regime: predictive abstraction yields embeddings that are both compact and well-separated regardless of cohort or modality.

Label-aware Clustering Agreement. Geometric metrics measure how cluster-like the embedding is; they do not measure whether the clusters correspond to clinical labels. We therefore add a label-aware analysis (Table 9): we run a 2-cluster KMeans on each embedding and measure agreement with ground-truth metabolic labels via ARI and NMI. The Initial cohort venous block reveals the clearest cross-view signal in the paper: X-CGM-JEPA achieves ARI 0.288 and NMI 0.249, against CGM-JEPA at 0.208 and 0.177, a relative improvement of +39% ARI and +40% NMI from the cross-view objective alone. PCA reaches ARI 0.225, also below X-CGM-JEPA. On the Validation cohort blocks, the three top embeddings (PCA, CGM-JEPA, X-CGM-JEPA) coincide on the same KMeans partition due to the small subject count and well-structured 2-cluster geometry, producing identical ARI/NMI; this is a

Table 10 | Per-patch label divergence: β -cell Dysfunction. Higher = more class-discriminative.

Encoder	P0 -10-45 m	P1 50-105 m	P2 110-165 m	P3 [†] 170-225 m
CGM-JEPA	0.009	0.159	0.161	0.014
X-CGM-JEPA	0.004	0.130	0.161	0.008

[†]P3 has only 3 real venous observations ($t = 170, 175, 180$); the remaining steps are flat-padded at the final glucose value, so P3 divergence is not directly comparable across patches.

Table 11 | Per-patch label divergence: Insulin Resistance. Higher = more class-discriminative.

Encoder	P0 -10-45 m	P1 50-105 m	P2 110-165 m	P3 [†] 170-225 m
CGM-JEPA	0.140	0.448	0.292	0.023
X-CGM-JEPA	0.109	0.373	0.288	0.012

[†]Same padding caveat as Table 10.

measurement-saturation artifact of small n rather than a genuine tie of representational quality, which the geometric metrics already differentiate. The location of the label-aware signal is itself informative: the Initial cohort venous block is precisely the regime in which the temporal view is sparsest, and it is exactly here that the auxiliary distributional view contributes label-aligned structure that the temporal-only encoder does not produce on its own.

Synthesis. The three families of metrics tell a consistent two-part story. The JEPA family produces geometrically stronger embeddings than every baseline across every cohort–modality block, supporting the consistency claim at the representation level. Within the JEPA family, the cross-view objective leaves its quantitatively largest fingerprint on label-aware clustering on the sparse Initial-cohort venous data, supporting the additive-abstraction claim: when the temporal view is data-thin, a complementary distributional view contributes structure that aligns the embedding more closely with clinical labels. These representation-level findings are consistent with the downstream patterns observed in Sections 2.1–2.3: the JEPA family delivers consistency across deployment regimes, while the cross-view extension contributes its most distinctive value where the temporal view is least informative.

2.5. Where Discriminative Signal Concentrates: Per-Patch Label Divergence

To localize *when* during the OGTT day the learned representations carry class-discriminative information, we compute per-patch label divergence: for each of the four post-meal temporal patches (P0–P3), we calculate the cosine distance between class-conditional mean embeddings on the test set. Higher divergence at a patch means the encoder distinguishes the two classes more sharply at that time window. Tables 10 and 11 report patch-wise divergence for the two endpoints.

Endpoint-specific Temporal Localization. The two endpoints exhibit visibly different patch-divergence profiles. For insulin resistance, divergence peaks at **P1 (50–105 min)**, the early post-load phase, with a secondary plateau at P2 (110–165 min). For β -cell dysfunction, divergence peaks instead at **P2**, with P1 already substantially above the early P0 baseline. The pattern is consistent across both encoders. This timing difference is consistent with what is known about the two failure modes physiologically: peripheral glucose-clearance impairment (IR) becomes apparent immediately after the glucose load, whereas inadequate insulin secretion (β -cell dysfunction) becomes more apparent once the response should be fully mobilized. We stress that this is a representation-level observation rather than a direct mechanistic test, but the agreement with prior physiological understanding

Table 12 | Venous-to-Home-CGM transfer: subgroup AUROCs, X-CGM-JEPA vs. CGM-JEPA. $\Delta = \text{X-CGM-JEPA} - \text{CGM-JEPA}$. All subgroups with $n \geq 5$ shown.

Endpoint	Subgroup	n	CGM-JEPA	X-CGM-JEPA	Δ
<i>β-cell Dysfunction</i>					
β	Ethn. Asian	5	0.739	0.792	+0.052
β	Sex = F	10	0.761	0.777	+0.016
β	Age 50–59	12	0.882	0.895	+0.013
β	BMI 18.5–24.9	6	0.962	0.972	+0.010
β	Sex = M	7	0.979	0.978	−0.001
β	Ethn. Caucasian	12	0.985	0.976	−0.009
β	BMI 25–29.9	6	0.999	0.984	−0.016
<i>Insulin Resistance</i>					
IR	Ethn. Asian	5	0.669	0.723	+0.054
IR	Sex = F	10	0.615	0.638	+0.023
IR	BMI 25–29.9	6	0.966	0.980	+0.014
IR	Ethn. Caucasian	12	0.753	0.762	+0.009
IR	Age 50–59	12	0.753	0.751	−0.002
IR	Sex = M	7	0.914	0.906	−0.009
IR	BMI 18.5–24.9	6	0.900	0.874	−0.025

indicates that the encoders are extracting label-relevant signal from clinically interpretable time windows rather than from spurious correlates.

Cross-view Effect on Temporal Localization. Comparing the two encoders, X-CGM-JEPA consistently shows *lower* peak per-patch divergence than CGM-JEPA (e.g., IR P1: 0.373 vs. 0.448). This is informative given that the two encoders achieve comparable downstream AUROC and that X-CGM-JEPA attains better F1 on the same task: lower per-patch divergence with equal or better thresholded performance suggests that the cross-view objective spreads class-discriminative signal more broadly across the day rather than concentrating it in a single patch. This pattern is consistent with the design intent of X-CGM-JEPA: by adding a distributional view that integrates evidence across the entire day, the cross-view objective discourages the encoder from leaning on any single time-window’s signature.

Limitations. Per-patch divergence is a coarse, patch-aggregated statistic on a small test cohort and does not establish a causal mechanism. P3 divergence values (Tables 10, 11) are particularly difficult to interpret due to the padding artifact noted in the footnote. We therefore present this analysis as suggestive rather than definitive evidence of the temporal physiological signature each endpoint elicits, and as a starting point for finer-grained interpretability work.

2.6. Demographic Subgroup Redistribution

Sections 2.1 and 2.2 established that X-CGM-JEPA matches CGM-JEPA on mean AUROC under deployment but contributes a consistent F1 advantage. We now examine where this F1 advantage comes from at the subgroup level. We stratify post-hoc test-set predictions in the two CGM deployment regimes (Home-CGM in-domain and Venous-to-Home-CGM transfer) by sex, age band, BMI category, and ethnicity, reporting AUROC for every subgroup with $n \geq 5$ subjects. The pattern is consistent across both regimes: the cross-view objective performs a worst-group-first redistribution, lifting subgroups where CGM-JEPA underperforms while leaving already-strong subgroups largely unchanged.

Table 13 | Home-CGM in-domain: subgroup AUROCs, X-CGM-JEPA vs. CGM-JEPA. All subgroups with $n \geq 5$ shown.

Endpoint	Subgroup	n	CGM-JEPA	X-CGM-JEPA	Δ
<i>Insulin Resistance</i>					
IR	Sex = F	10	0.529	0.570	+0.040
IR	BMI 25–29.9	6	0.954	0.985	+0.031
IR	Age 50–59	12	0.747	0.770	+0.023
IR	Ethn. Caucasian	12	0.752	0.769	+0.016
IR	Ethn. Asian	5	0.716	0.733	+0.016
IR	Sex = M	7	0.973	0.971	−0.002
IR	BMI 18.5–24.9	6	0.973	0.967	−0.006
<i>β-cell Dysfunction (near-saturated)</i>					
β	Sex = F	10	0.709	0.714	+0.005
β	Age 50–59	12	0.883	0.888	+0.005
β	Ethn. Asian	5	0.783	0.787	+0.005
β	Sex = M	7	0.999	0.999	0.000
β	BMI 18.5–24.9	6	1.000	1.000	0.000
β	BMI 25–29.9	6	1.000	1.000	0.000
β	Ethn. Caucasian	12	1.000	0.995	−0.005

Cross-modality Transfer. Under transfer (Table 12), the largest X-CGM-JEPA gains concentrate on the subgroups where CGM-JEPA is weakest. On both endpoints, the Asian-ethnicity subgroup, which has the lowest CGM-JEPA AUROC (0.739 on β -cell, 0.669 on IR), receives the largest boost (+0.052 and +0.054 respectively). The female subgroup also improves on both endpoints (+0.016 on β -cell, +0.023 on IR), again starting from below the model’s average performance. Offsetting decrements appear on already-strong majority subgroups (Caucasian- β −0.009, BMI 25–29.9 β −0.016, BMI 18.5–24.9 IR −0.025), but in absolute terms these subgroups remain at AUROC > 0.87.

The aggregate effect is a compression of the subgroup performance distribution rather than a uniform lift. The maximum-to-minimum ethnicity AUROC gap shrinks by 25% on β -cell (0.246 → 0.184) and 54% on IR (0.084 → 0.039). Sex gaps shrink by 8% (β -cell) and 10% (IR). Mean AUROC across subgroups changes by less than +0.01 on both endpoints. The cross-view objective therefore does not raise the average; it compresses the worst-to-best spread.

In-domain Home CGM. The same redistribution pattern appears in the home in-domain regime (Table 13), most clearly on insulin resistance. The female subgroup, on which CGM-JEPA performs near-chance (0.529), receives the largest X-CGM-JEPA lift (+0.040) and crosses above 0.57, while male performance, at ceiling for CGM-JEPA (0.973), remains essentially unchanged (−0.002). The IR sex gap shrinks from 0.444 to 0.401 (a 10% reduction). Both ethnicity subgroups improve symmetrically (+0.016). The β -cell endpoint is near-saturated in the home regime (≥ 0.99 on five of seven subgroups for both methods), so all β -cell deltas in this table fall within run-to-run noise and we draw no inference from them.

Caveats. Per-subgroup sample sizes are small ($n = 5$ to 12), and individual cell AUROCs should be read with appropriate caution; we report all subgroups meeting $n \geq 5$ to avoid selection. The *pattern* is robust across 20 iterations \times 2-fold cross-validation: across both regimes and both endpoints, the largest X-CGM-JEPA gains land on subgroups where CGM-JEPA is weakest, and the largest decrements land on subgroups already near ceiling. The redistribution is consistent with the additive-cross-view design: the Glucodensity view supplies complementary structure that disproportionately benefits subgroups whose temporal patterns alone are harder for the encoder to separate, providing a deployment-relevant fairness property that the AUROC means do not capture.

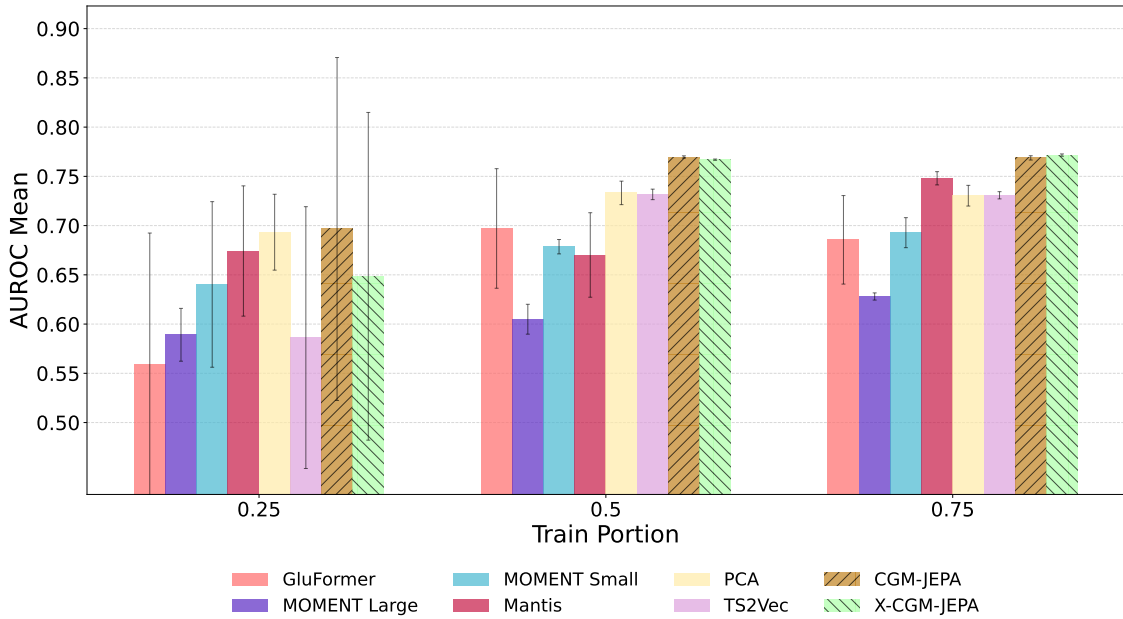
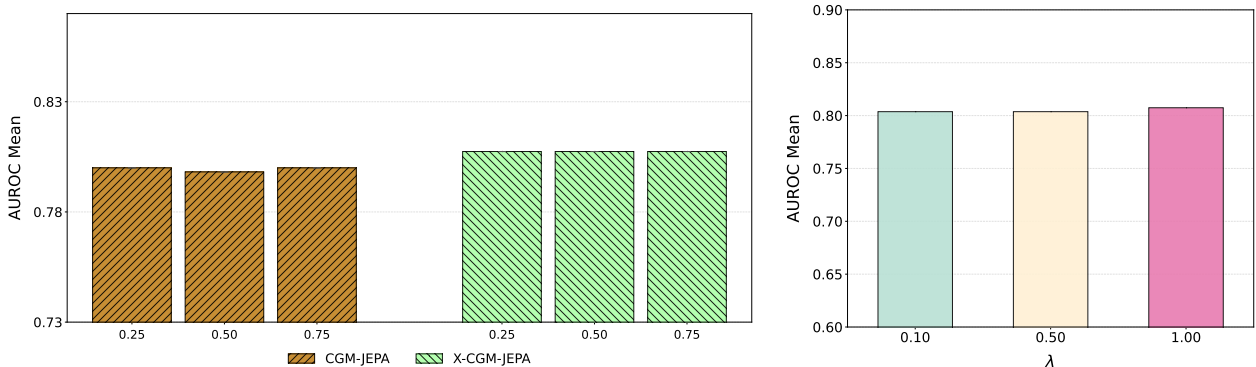


Figure 2 | Comparison across different training portions.

3. Ablation Studies



(a) CGM-JEPA and X-CGM-JEPA: masking ratio sensitivity.

(b) X-CGM-JEPA: cross-view weight λ sensitivity.Figure 3 | Hyperparameter sensitivity of the JEPA family. (a) AUROC across masking ratios for both encoders. (b) X-CGM-JEPA sensitivity to the cross-view weight λ .

Effect of Label Availability. Figure 2 reports AUROC and run-to-run standard deviation across labeled-data portions (25%, 50%, 75%). The picture has two distinct regimes. At the 25% portion (very few labeled subjects), all eight encoders sit within a noisy band: CGM-JEPA is nominally first (0.697) and PCA second (0.693), but the standard deviations are large for several methods (CGM-JEPA 0.174, X-CGM-JEPA 0.166, TS2VEC 0.133, GLUFORMER 0.134), reflecting how little training signal is available at this portion rather than a property of the encoders themselves. We do not draw rank-level conclusions in this regime.

Once labels reach 50% or 75%, the picture stabilizes sharply and the JEPA family separates from the rest. At 50%: CGM-JEPA 0.770 ± 0.001 and X-CGM-JEPA 0.767 ± 0.001 are first and second, with the strongest baseline (PCA) at 0.733 ± 0.012 . At 75%: X-CGM-JEPA 0.772 ± 0.001 and CGM-JEPA 0.769 ± 0.002 remain first and second; the next baseline (Mantis) reaches 0.748 ± 0.007 . Two patterns

are notable. First, the JEPA family consistently outperforms all baselines by 2 to 4 AUROC points whenever the data regime is informative enough to draw conclusions. Second, the JEPA family’s run-to-run standard deviation is one to two orders of magnitude smaller than the strongest baselines at 50% and 75% (e.g., 0.0007 vs. PCA 0.012 at 50%), indicating that abstraction-first pretraining yields representations whose performance is highly reproducible across folds once supervision is sufficient to identify the embedding’s discriminative structure.

Effect of Masking Ratio. We sweep the pretraining masking ratio over {25%, 50%, 75%} for both encoders (Figure 3a). AUROC is essentially flat: CGM-JEPA mean varies within 0.001 across the three ratios, and X-CGM-JEPA produces identical mean AUROC (0.805) at all three. Run-to-run standard deviations are also small in absolute terms (0.002–0.007), and X-CGM-JEPA is approximately 2.7× more stable than CGM-JEPA at every ratio (0.0021 vs. 0.0057 on average). The flat behavior indicates that day-level CGM windows carry sufficient temporal redundancy for simple random masking to provide a reliable pretraining signal across a wide range, and the cross-view objective reduces variance further without altering the central tendency. We use 25% masking in all main results on this basis.

Effect of Cross-view Weight λ . Figure 3b reports X-CGM-JEPA AUROC at $\lambda \in \{0.1, 0.5, 1.0\}$, averaged across masking ratios. Mean AUROC ranges over [0.7730, 0.7745], a spread of 0.0016, while the run-to-run standard deviation at each λ is 0.043–0.046, more than an order of magnitude larger than the mean spread. Differences across λ are therefore well within fold-to-fold variability, and the three settings are not distinguishable in this dataset. The robustness is consistent with the additive-abstraction interpretation: the Glucodensity view contributes complementary structure rather than competing with the temporal objective, so the encoder is not destabilized by varying their relative weight. We fix $\lambda=1$ in all main results.

4. Discussion

Limitations. Our study leverages a clinically curated cohort that provides two forms of *gold-standard* information: (i) *gold-standard sample collection* via venous blood draws during an in-clinic OGTT, and (ii) *gold-standard condition labels* (insulin resistance and β -cell dysfunction) derived from these assessments. Because OGTT-based protocols are costly and invasive, such high-fidelity labels are rarely available at scale; accordingly, our dataset serves as a high-quality benchmark for studying label-efficient CGM representation learning. Despite explicitly evaluating distribution shifts (e.g., venous-to-CGM and controlled-to-home), our experiments are still tied to a specific data-collection pipeline and sensor modality. Real-world deployment may introduce additional shifts (e.g., device calibration, missingness patterns) and subgroup-dependent performance. While we reduce overfitting and leakage via cohort hold-out evaluation, stratified cross-validation, and fold-wise normalization, limited subgroup metadata prevents comprehensive fairness analysis; larger multi-site, multi-device cohorts are needed for robust validation and bias assessment.

Conclusion. We studied metabolic dysfunction prediction from continuous glucose monitoring (CGM) under three clinically motivated settings: controlled venous evaluation with cohort generalization, venous-to-CGM transfer, and real-world home CGM evaluation. We introduced CGM-JEPA, a predictive self-supervised pretraining framework tailored to day-level CGM windows, and X-CGM-JEPA, which further regularizes CGM representations via an auxiliary cross-view Glucodensity prediction objective. Across experiments, predictive pretraining yields strong and label-efficient representations, while the cross-view extension provides the most consistent benefits under clinically

relevant distribution shifts, particularly in venous-supervised deployment where inference relies on wearable CGM. In contrast, in-domain home evaluation exhibits limited headroom over strong baselines, suggesting that the main value of cross-view guidance lies in improving transferability rather than maximizing in-domain accuracy.

Our results highlight the promise of predictive self-supervision for extracting clinically meaningful structure from consumer-grade CGM with scarce gold-standard labels. Future work will extend cross-view objectives to richer physiological signals and larger cohorts, and investigate uncertainty-aware deployment for individualized metabolic risk assessment.

References

- [1] Abdul Fatir Ansari, Lorenzo Stella, Caner Turkmen, Xiyuan Zhang, Pedro Mercado, Huibin Shen, Oleksandr Shchur, Syama Sundar Rangapuram, Sebastian Pineda Arango, Shubham Kapoor, Jasper Zschiegner, Danielle C. Maddix, Hao Wang, Michael W. Mahoney, Kari Torkkola, Andrew Gordon Wilson, Michael Bohlke-Schneider, and Yuyang Wang. Chronos: Learning the language of time series. *Transactions on Machine Learning Research*, 2024.
- [2] Mahmoud Assran, Quentin Duval, Ishan Misra, Piotr Bojanowski, Pascal Vincent, Michael Rabbat, Yann LeCun, and Nicolas Ballas. Self-supervised learning from images with a joint-embedding predictive architecture. In *Proceedings of the IEEE/CVF Conference on Computer Vision and Pattern Recognition*, pages 15619–15629, 2023.
- [3] Mahmoud Assran, Quentin Duval, Ishan Misra, Piotr Bojanowski, Pascal Vincent, Michael Rabbat, Yann LeCun, and Nicolas Ballas. Self-supervised learning from images with a joint-embedding predictive architecture, 2023.
- [4] Baiyu Chen, Wilson Wongso, Zechen Li, Yonchanok Khaokaew, Hao Xue, and Flora Salim. Co-modo: Cross-modal video-to-imu distillation for efficient egocentric human activity recognition, 2025.
- [5] Delong Chen, Mustafa Shukor, Theo Moutakanni, Willy Chung, Jade Yu, Tejaswi Kasarla, Allen Bolourchi, Yann LeCun, and Pascale Fung. Vl-jepa: Joint embedding predictive architecture for vision-language. *arXiv preprint arXiv:2512.10942*, 2025.
- [6] Ting Chen, Simon Kornblith, Mohammad Norouzi, and Geoffrey Hinton. A simple framework for contrastive learning of visual representations. In *Proceedings of the 37th International Conference on Machine Learning*, ICML’20. JMLR.org, 2020.
- [7] Ana Colás, Luis Vigil, Borja Vargas, David Cuesta-Frau, and Manuel Varela. Detrended fluctuation analysis in the prediction of type 2 diabetes mellitus in patients at risk: Model optimization and comparison with other metrics. *PloS one*, 14(12):e0225817, 2019.
- [8] Abhimanyu Das, Weihao Kong, Rajat Sen, and Yichen Zhou. A decoder-only foundation model for time-series forecasting. In *Proceedings of the 41st International Conference on Machine Learning*, ICML’24. JMLR.org, 2024.
- [9] Zijian Dong, Ruilin Li, Yilei Wu, Thuan Tinh Nguyen, Joanna Chong, Fang Ji, Nathanael Tong, Christopher Chen, and Juan Helen Zhou. Brain-jepa: Brain dynamics foundation model with gradient positioning and spatiotemporal masking. *Advances in Neural Information Processing Systems*, 37:86048–86073, 2024.

- [10] Vasilii Feofanov, Songkang Wen, Marius Alonso, Romain Ilbert, Hongbo Guo, Malik Tiomoko, Lujia Pan, Jianfeng Zhang, and Ievgen Redko. Mantis: Lightweight calibrated foundation model for user-friendly time series classification, 2025.
- [11] Ian Fox, Lynn Ang, Mamta Jaiswal, Rodica Pop-Busui, and Jenna Wiens. Contextual motifs: Increasing the utility of motifs using contextual data. In *Proceedings of the 23rd ACM SIGKDD International Conference on Knowledge Discovery and Data Mining, KDD '17*, page 155–164, New York, NY, USA, 2017. Association for Computing Machinery.
- [12] Mononito Goswami, Konrad Szafer, Arjun Choudhry, Yifu Cai, Shuo Li, and Artur Dubrawski. Moment: A family of open time-series foundation models. In *International Conference on Machine Learning*, 2024.
- [13] Kaiming He, Haoqi Fan, Yuxin Wu, Saining Xie, and Ross Girshick. Momentum contrast for unsupervised visual representation learning. In *2020 IEEE/CVF Conference on Computer Vision and Pattern Recognition (CVPR)*, pages 9726–9735, 2020.
- [14] Ashish Jaiswal, Ashwin Ramesh Babu, Mohammad Zaki Zadeh, Debapriya Banerjee, and Fillia Makedon. A survey on contrastive self-supervised learning, 2021.
- [15] David C Klonoff, Richard M Bergenstal, Eda Cengiz, Mark A Clements, Daniel Espes, Juan Espinoza, David Kerr, Boris Kovatchev, David M Maahs, Julia K Mader, et al. Continuous glucose monitoring data analysis 2.0: functional data pattern recognition and artificial intelligence applications. *Journal of Diabetes Science and Technology*, 19(6):1515–1527, 2025.
- [16] Zechen Li, Baiyu Chen, Hao Xue, and Flora D. Salim. Zara: Zero-shot motion time-series analysis via knowledge and retrieval driven llm agents. *arXiv preprint arXiv:2508.04038*, 2025.
- [17] Zechen Li, Shohreh Deldari, Linyao Chen, Hao Xue, and Flora D. Salim. SensorLLM: Aligning large language models with motion sensors for human activity recognition. In *Proceedings of the 2025 Conference on Empirical Methods in Natural Language Processing*, pages 354–379, 2025.
- [18] Yurun Lu, Dan Liu, Zhongming Liang, Rui Liu, Pei Chen, Yitong Liu, Jiachen Li, Zhanying Feng, Lei M Li, Bin Sheng, et al. A pretrained transformer model for decoding individual glucose dynamics from continuous glucose monitoring data. *National Science Review*, 12(5):nwaf039, 2025.
- [19] Junjie Luo, Abhimanyu B Kumbara, Mansur Shomali, Rui Han, Anand Iyer, Grazia Aleppo, Ritu Agarwal, and Gordon Gao. A large sensor foundation model pretrained on continuous glucose monitor data for diabetes management. *npj Health Systems*, 2, 2024.
- [20] Guy Lutsker, Gal Sapir, Smadar Shilo, Jordi Merino, Anastasia Godneva, Jerry R Greenfield, Dorit Samocha-Bonet, Raja Dhir, Francisco Gude, Shie Mannor, et al. Gluformer: Learning generalizable representations from continuous glucose monitoring data. In *Learning Meaningful Representations of Life (LMRL) Workshop at ICLR 2025*.
- [21] Marcos Matabuena, Rahul Ghosal, Javier Enrique Aguilar, Ayya Keshet, Robert Wagner, Carmen Fernández Merino, Juan Sánchez Castro, Vadim Zipunnikov, Jukka-Pekka Onnela, and Francisco Gude. Glucodensity functional profiles outperform traditional continuous glucose monitoring metrics. *Scientific reports*, 15(1):33662, 2025.
- [22] Ahmed A Metwally, Heyjun Park, Yue Wu, Tracey McLaughlin, and Michael P Snyder. Use of continuous glucose monitoring with machine learning to identify metabolic subphenotypes and inform precision lifestyle changes. *Journal of Diabetes Science and Technology*, 2025.

- [23] Ahmed A Metwally, Dalia Perelman, Heyjun Park, Yue Wu, Alok Kumar Jha, Seth Sharp, Alessandra Celli, Ekrem Ayhan, Fahim Abbasi, Anna L Gloyn, et al. Prediction of metabolic subphenotypes of type 2 diabetes via continuous glucose monitoring and machine learning. *Nature biomedical engineering*, 9(8):1222–1239, 2025.
- [24] Yuqi Nie, Nam H. Nguyen, Phanwadee Sinthong, and Jayant Kalagnanam. A time series is worth 64 words: Long-term forecasting with transformers. In *International Conference on Learning Representations*, 2023.
- [25] Heyjun Park, Ahmed A. Metwally, Alireza Delfarah, Yue Wu, Dalia Perelman, Caleb Mayer, Curtis McGinity, Majid Rodgar, Alessandra Celli, Tracey McLaughlin, Emmanuel Mignot, and Michael Snyder. High-resolution lifestyle profiling and metabolic subphenotypes of type 2 diabetes. *npj Digital Medicine*, 8(352), 2025.
- [26] Renat Sergazinov, Elizabeth Chun, Valeriya Rogovchenko, Nathaniel Fernandes, Nicholas Kasman, and Irina Gaynanova. Glucobench: Curated list of continuous glucose monitoring datasets with prediction benchmarks, 2024.
- [27] Jonathon Shlens. A tutorial on principal component analysis, 2014.
- [28] Kuba Weimann and Tim OF Conrad. Self-supervised pre-training with joint-embedding predictive architecture boosts ecg classification performance. *Computers in Biology and Medicine*, 196:110809, 2025.
- [29] Yue Wu, Ben Ehlert, Ahmed A Metwally, Dalia Perelman, Heyjun Park, Andrew Wallace Brooks, Fahim Abbasi, Basil Michael, Alessandra Celli, Caroline Bejikian, Ekrem Ayhan, Yingzhou Lu, Samuel M. Lancaster, Daniel Hornburg, Lucia Ramirez, David Bogumil, Sarah Pollock, Frank Wong, Denver Bradley, Georg Gutjahr, Ekanath Srihari Rangan, Tao Wang, Lettie McGuire, P. Venkat Rangan, and Michael P. Snyder. Individual variations in glycemic responses to carbohydrates and underlying metabolic physiology. *Nature medicine*, 31(7):2232–2243, 2025.
- [30] Zhihan Yue, Yujing Wang, Juanyong Duan, Tianmeng Yang, Congrui Huang, Yunhai Tong, and Bixiong Xu. Ts2vec: Towards universal representation of time series, 2022.
- [31] Yuwei Zhang, Kumar Ayush, Siyuan Qiao, A. Ali Heydari, Girish Narayanswamy, Maxwell A. Xu, Ahmed A. Metwally, Shawn Xu, Jake Garrison, Xuhai Xu, Tim Althoff, Yun Liu, Pushmeet Kohli, Jiening Zhan, Mark Malhotra, Shwetak Patel, Cecilia Mascolo, Xin Liu, Daniel McDuff, and Yuzhe Yang. Sensorlm: Learning the language of wearable sensors, 2025.
- [32] Meng Zhou, Zechen Li, and Pengtao Xie. Self-supervised regularization for text classification. *Transactions of the Association for Computational Linguistics*, 9:641–656, 2021.

Methods

M.2. Related Work

CGM-Based Metabolic Subphenotype Prediction. Prior studies have demonstrated that continuous glucose monitoring (CGM) data can be leveraged to predict clinically meaningful metabolic subphenotypes using supervised machine learning. In particular, [23] shows that CGM-derived features can be used to infer insulin resistance and β -cell dysfunction when paired with gold-standard venous glucose measurements. While effective, such approaches rely on fully supervised learning and require access to high-quality metabolic labels, which are expensive and invasive to obtain. Consequently, their applicability is limited in large-scale or real-world settings where labeled data are scarce.

Functional Representations of Glucose Dynamics. Beyond conventional summary statistics, functional representations of CGM have been proposed to better characterize glucose dynamics. Glucodensity-based methods model glucose trajectories through distributional profile, capturing the statistical structure of glucose fluctuations over time rather than point-wise values [15]. Empirical evidence suggests that glucodensity functional profiles can outperform traditional CGM metrics in downstream characterization tasks [21]. These findings highlight glucodensity as a complementary view of glucose regulation, motivating its use alongside raw CGM signals to capture physiologically relevant dynamics.

Self-Supervised Learning for CGM Time Series. Self-supervised learning has recently emerged as a promising approach for learning CGM representations without extensive labeled annotations. GLU-FORMER [20] pretrains models with autoregressive and reconstruction-style objectives, emphasizing point-wise signal fidelity and capturing short-term glucose dynamics. In parallel, CGM_{FORMER} [18] leverages large-scale CGM pretraining to learn individualized glucose representations and demonstrates improved generalization across downstream tasks.

Time Series Foundation Model. Beyond CGM-specific SSL, recent time-series foundation models pretrained on large, multi-domain corpora aim to provide transferable representations with strong out-of-the-box performance on downstream tasks. Representative examples include MOMENT [12] and Mantis [10] for general representation learning and classification, as well as forecasting-oriented pretrained models such as TimesFM [8] and Chronos [1]. Related sensor-based language models have also been proposed for wearable and physiological data [16, 17, 31]. While these models benefit from scale and broad coverage, their pretraining data and objectives are not tailored to CGM’s physiology-driven dynamics or to device-specific noise, missingness, and sampling irregularities.

M.3. Methodology

M.3.1. Problem Setup

For each subject i , we observe a CGM time series $\mathbf{X}_i = \{g_{i1}, \dots, g_{iT_i}\}$, where $g_{it} \in \mathbb{R}$ is the glucose value recorded at the t -th timestamp. A subset of subjects has gold-standard metabolic labels for two binary outcomes: insulin resistance and β -cell dysfunction. Our goal is to learn an encoder f_θ that maps a CGM window to a fixed-dimensional embedding $\mathbf{z}_i = f_\theta(\mathbf{X}_i) \in \mathbb{R}^d$, enabling a lightweight classifier h_ϕ to predict these outcomes with limited supervision. Because labeled metabolic assessments are scarce, we learn f_θ via self-supervised pretraining on unlabeled CGM and evaluate representation quality via linear probing.

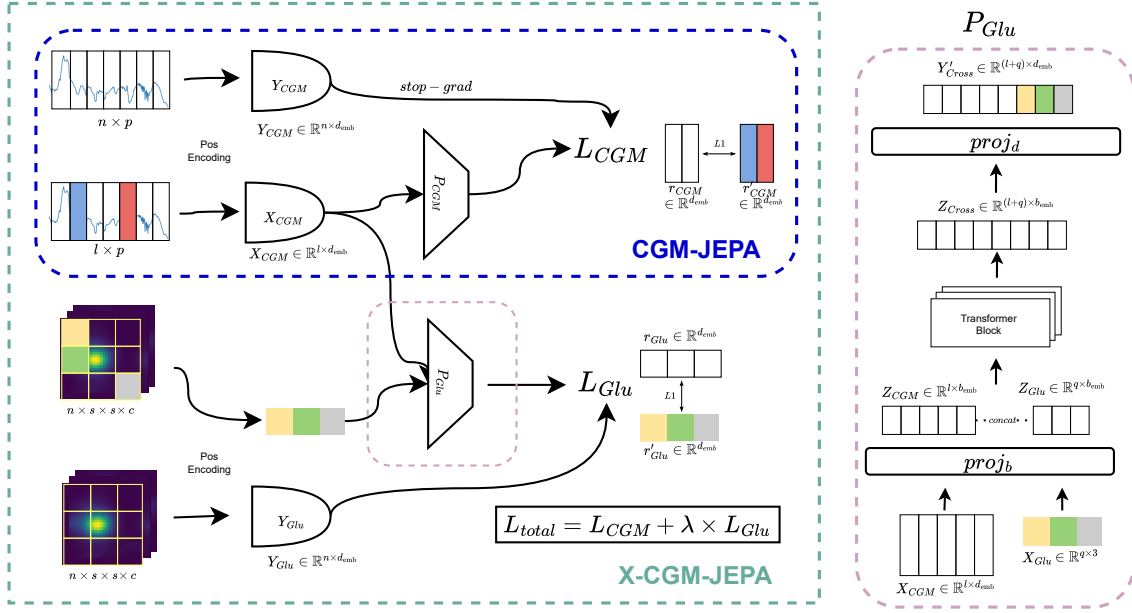


Figure ED.1 | Overview of our predictive pretraining framework for CGM. CGM-JEPA learns representations by predicting masked CGM patch embeddings from visible context. X-CGM-JEPA extends CGM-JEPA with an auxiliary cross-view objective that predicts a masked Glucodensity embedding derived from the same day window.

M.3.2. CGM Windowing and Tokenization

We segment each CGM stream into daily windows of length 288 (5-minute sampling). Each day is tokenized into $P = 24$ non-overlapping hourly patches with patch size 12. Let $\mathbf{x} \in \mathbb{R}^{P \times 12}$ denote a tokenized day. This patchified representation standardizes temporal resolution and supports patch-level masking for predictive pretraining.

M.3.3. Predictive Pretraining on CGM: CGM-JEPA

We first introduce CGM-JEPA, a JEPA-style predictive representation learner tailored to CGM. Rather than reconstructing raw glucose values, CGM-JEPA performs *masked representation prediction*: it predicts the latent representations of masked patches from the visible context, encouraging the encoder to capture higher-level temporal structure.

M.3.3.1. Masked context–target construction.

Given a tokenized day $\mathbf{x} \in \mathbb{R}^{P \times 12}$, we sample a patch mask $\mathcal{M} \subseteq \{1, \dots, P\}$ and form a context view $\mathbf{x}^{(c)}$ by retaining only visible patches, while the target view corresponds to the masked patch indices \mathcal{M} . A context encoder f_θ encodes the visible context, and a target encoder $f_{\bar{\theta}}$ encodes the target view:

$$\mathbf{z}^{(c)} = f_\theta(\mathbf{x}^{(c)}), \quad \mathbf{z}^{(t)} = f_{\bar{\theta}}(\mathbf{x}),$$

where $\mathbf{z}^{(t)} = \{\mathbf{z}_j^{(t)}\}_{j=1}^P$ provides per-patch target representations and only $\{\mathbf{z}_j^{(t)}\}_{j \in \mathcal{M}}$ are used as prediction targets. A predictor p_ϕ maps the context embedding to predicted representations for the masked indices:

$$\hat{\mathbf{z}}^{(t)} = p_\phi(\mathbf{z}^{(c)}), \quad \hat{\mathbf{z}}^{(t)} = \{\hat{\mathbf{z}}_j^{(t)}\}_{j \in \mathcal{M}}.$$

We minimize an ℓ_1 (MAE) regression loss between predicted and target representations over masked patches, stopping gradients on the target branch:

$$\mathcal{L}_{\text{CGM}} = \frac{1}{|\mathcal{M}|} \sum_{j \in \mathcal{M}} \left\| \hat{\mathbf{z}}_j^{(t)} - \text{stopgrad}(\mathbf{z}_j^{(t)}) \right\|_1.$$

This objective yields a predictive SSL framework for CGM that can be trained on abundant unlabeled home CGM.

M.3.4. Cross-view Regularization: X-CGM-JEPA

While CGM-JEPA focuses on temporal structure in the 1D trajectory, CGM windows also exhibit clinically meaningful distributional patterns (e.g., variability and density over time). To capture complementary distributional structure, especially under modality or setting shifts, we propose X-CGM-JEPA, which augments CGM-JEPA with an auxiliary cross-view prediction objective based on a Glucodensity representation.

M.3.4.1. Glucodensity view.

From the same daily CGM window, we derive a Glucodensity representation \mathbf{D} using our preprocessing pipeline. \mathbf{D} is a deterministic transformation that summarizes distributional structure of glucose dynamics over the day. We patchify \mathbf{D} into tokens and apply patch-level masking, denoting the masked Glucodensity tokens by $\mathbf{D}^{(t)}$. A Glucodensity encoder g_ψ maps the masked Glucodensity tokens to an embedding:

$$\mathbf{u} = g_\psi(\mathbf{D}^{(t)}).$$

M.3.4.2. Asymmetric cross-view prediction.

Using the CGM context embedding $\mathbf{z}^{(c)}$, a cross-view predictor q_ω predicts the masked Glucodensity embedding:

$$\hat{\mathbf{u}} = q_\omega(\mathbf{z}^{(c)}), \quad \mathcal{L}_{\text{GD}} = \|\hat{\mathbf{u}} - \mathbf{u}\|_1.$$

Here, Glucodensity is used as an auxiliary *target*, and masking is applied to mitigate shortcuts from full-window summaries. Unlike the CGM target branch, gradients are allowed to flow into g_ψ so that the Glucodensity encoder is learned jointly through the auxiliary objective.

M.3.4.3. Overall objective.

X-CGM-JEPA combines the CGM predictive loss with the cross-view Glucodensity loss:

$$\mathcal{L}_{\text{total}} = \mathcal{L}_{\text{CGM}} + \lambda \mathcal{L}_{\text{GD}},$$

where λ is a nonnegative coefficient that balances the cross-view Glucodensity objective against the CGM predictive objective. We fix $\lambda=1$ in the main experiments and analyze sensitivity to λ in the ablation study.

M.3.5. Downstream Evaluation Protocol

After pretraining, we freeze the CGM encoder f_θ and extract embeddings for labeled subjects. We then train simple a linear classifier head (logistic regression) on top of embeddings for both insulin resistance β -cell dysfunction. We report AUROC, PRAUC, and F1 under multiple evaluation settings, including controlled in-clinic venous evaluation, venous-to-CGM cross-modality transfer, and in-domain home CGM evaluation.

M.4. Dataset Overview

We use two complementary CGM corpora: an unlabeled corpus assembled for self-supervised pretraining and a labeled corpus, with paired venous and continuous-glucose measurements, for downstream metabolic-subphenotype evaluation.

M.4.1. Pretraining Sensor Dataset

The pretraining corpus pools two open CGM cohorts into a single unlabeled stream of 5-minute glucose readings:

- **Stanford initial cohort.** 22 subjects from the Stanford CGM study [23] who carry continuous CGM data in the released file (the remaining 5 subjects of the initial cohort have only OGTT measurements and are excluded).
- **Colas CGM [7].** 206 subjects whose recordings are sliced into full-day windows, yielding 391 daily samples.

After cohort merging, the pretraining table contains **413 subject-days** ($\approx 389,365$ rows at 5-minute resolution). Streams are segmented into 24-hour windows of length 288, with optional sliding stride (288 = no overlap; 144 = 50% overlap). All windows are tokenized into $P=24$ non-overlapping hourly patches of size 12 prior to encoding. Glucodensity views used by X-CGM-JEPA are pre-computed once per window via Gaussian KDE on a 32×32 grid and patchified spatially with patch size 8. No subject-level normalization is applied to the input glucose values in the default configuration.

M.4.2. Downstream Datasets

Downstream evaluation uses the labeled subset of the Stanford CGM study [23] with metabolic phenotypes derived from gold-standard clinical assays:

- **Insulin Resistance (IR).** Binary label derived from `sspg_2_classes` (steady-state plasma glucose dichotomized into Insulin-Resistant vs. Insulin-Sensitive).
- **β -cell dysfunction (Beta).** Binary label derived from `di_2_classes_median` (median-split of the disposition index into Dysfunction vs. Normal).

We adopt the Stanford-released cohort partitioning into two splits, distinguished by the presence of paired at-home CGM:

- **Initial cohort (train, $n=27$).** Subjects with *venous OGTT only* (no matching CGM, no planned at-home CGM). Each entry contains a single `ctru_venous` OGTT trace of 39 glucose values at 5-minute intervals spanning $t=-10$ to $t=180$ minutes, smoothed with a smoothing spline at $\lambda=0.35$ with internal -1 gaps interpolated.
- **Validation cohort ($n=17$).** Subjects with *paired venous OGTT and at-home CGM*, after removing dual-cohort overlaps with the initial cohort. Each entry exposes six aligned extraction methods: `ctru_venous` (in-clinic venous), `ctru_cgm` (in-clinic CGM during the OGTT), `home_cgm_1` and `home_cgm_2` (two at-home CGM sessions), `cgm_home_mean` (mean of the two home sessions), and `cgm_all_mean` (mean of `ctru_cgm`, `home_cgm_1`, `home_cgm_2`). Smoothing uses $\lambda=0.4$.

For reference, the exact `exp_type` flag values used to filter the upstream Stanford release are:

Cohort	exp_type flag
Initial	venous_without_matching_cgm_and_without_planned_athome_cgm
Validation	venous_with_matching_cgm_and_with_planned_athome_cgm

The combination of split type and extraction method defines the three evaluation pipelines reported in the main paper: in-clinic venous (`ctru_venous` \rightarrow `ctru_venous`), cross-modality transfer (`ctru_venous` \rightarrow `home_cgm_mean`), and in-domain home CGM (`cgm_home_mean` \rightarrow `cgm_home_mean`).

M.4.3. Sampling Rates and Preprocessing

The downstream cohort exposes two physically distinct acquisition modalities, *venous OGTT* (clinical phlebotomy) and *CGM* (subcutaneous interstitial sensor), which arrive at different cadences. We homogenize all streams onto a common 5-minute grid via a single shared alignment and smoothing pipeline, but the effect of that pipeline differs by modality, as we describe below.

Common alignment grid. For every subject and every extraction method, we instantiate a 5-minute grid spanning $t = -10$ to $t = 180$ minutes (39 positions). For each grid position, we look up an exact-timepoint match in the source (`Timepoint`, `Glucose`) table; if no observation exists at that exact timepoint, the slot is filled with a sentinel value of -1 . We deliberately do *not* round neighboring timepoints onto the grid, so unaligned acquisitions remain marked as missing.

Venous OGTT: irregular and sparse. The `ctru_venous` stream consists of clinical phlebotomy draws at the Stanford Clinical Translational Research Unit during a standard oral glucose tolerance test (OGTT). Native acquisition times are the OGTT clinical sampling timepoints (typically $t \in \{-10, 0, 15, 30, 60, 90, 120, 150, 180\}$ minutes), so only ~ 9 of the 39 grid slots receive an observation; the remaining ~ 30 slots are sentinel-filled. To recover a usable 5-minute trace, we fit a non-parametric smoothing spline via `scipy.interpolate.make_smoothing_spline` on the non-sentinel positions, then evaluate the fitted spline at *all* 39 grid positions; sentinel positions therefore receive interpolated values on output. We use regularization $\lambda = 0.35$ for the initial cohort and $\lambda = 0.4$ for the validation cohort. Because the venous trace is sparse to begin with, the spline here is doing *interpolation under denoising*, and the fitted curve is the only object the model ever sees from the venous channel.

CGM: natively 5-minute aligned. CGM streams (`ctru_cgm`, `home_cgm_1`, `home_cgm_2`) are acquired at the sensor’s native 5-minute cadence and therefore land directly on the alignment grid: nearly all 39 positions receive a real observation, and very few sentinels are produced. We pass these streams through the same alignment and smoothing pipeline as the venous channel for a uniform interface; with the CGM streams the spline is effectively denoising only, since there are no large gaps to interpolate. Two derived “mean” streams used in our cross-modality experiments are pointwise averages over only the components that have a value at each grid position:

$$\begin{aligned} \text{cgm_home_mean}_t &= \text{mean}\{\text{home_cgm_1}_t, \text{home_cgm_2}_t\}, \\ \text{cgm_all_mean}_t &= \text{mean}\{\text{ctru_cgm}_t, \text{home_cgm_1}_t, \text{home_cgm_2}_t\}. \end{aligned}$$

A small number of subjects (e.g., S80) lack one of the at-home sessions; for those subjects the missing component is simply omitted from the mean rather than imputed. `cgm_all_mean` provides a single, denoised CGM trajectory per subject and is the canonical *val_extract_method* for the in-domain home CGM evaluation in the main paper.

M.4.4. Data Acquisition and Approval

All data used in this work are derived from publicly released CGM corpora. The Stanford CGM study and its labeled metabolic subphenotypes are distributed via the [Metabolic_Subphenotype_Predictor](#) repository, and the Colas et al. CGM dataset is released by the original authors. Both sources retain their original IRB approvals and de-identification protocols; no additional human-subject data were collected for this work, and our preprocessing only operates on already de-identified glucose traces. We release the merged, preprocessed dataset (Dataset_Open/) together with the train/validation split files used in our experiments to support reproducibility.

M.5. Implementation Details

M.5.1. Model Architecture

The CGM context encoder f_θ is a lightweight Transformer over patch tokens. Each hourly patch of size 12 is mapped to an embedding via a 1D convolutional patch embedder with kernel size 3 and bias enabled. Embedded patches pass through a stack of standard pre-norm Transformer blocks, after which optional sinusoidal time features can be appended (disabled by default to avoid embedding mismatch with downstream sets that lack timestamps). The target encoder $f_{\hat{\theta}}$ shares the architecture of f_θ and is updated by an exponential moving average (EMA) of f_θ . The masked-patch predictor p_ϕ is a smaller Transformer operating on positional-conditioned context tokens.

Component	Hyperparameter	Value
Patch embedder	patch size / conv kernel	12 / 3
Context encoder	embed dim / heads / layers	96 / 6 / 3
Context encoder	embed bias / dropout	True / 0.0
Target encoder	EMA momentum	0.997
Predictor	embed dim / heads / layers	48 / 2 / 1
Glucodensity	KDE grid / spatial patch size	32×32 / 8
Window	length / patches per window	288 / 24

Table ED.1 | CGM-JEPA / X-CGM-JEPA architecture defaults.

M.5.2. Pretraining Details

We pretrain on day-windowed CGM with patch-level masking. The default mask ratio is 0.25 (varied in the ablation study), and the cross-view weight λ is fixed to 1.0 in the main results. Optimization uses Adam with learning rate 10^{-4} , an exponential learning-rate schedule (`step_size` = 100, `gamma` = 0.99), a warmup ratio of 0.15, gradient norm clipping at 1.0, and an iteration-per-epoch scaling factor `ipe_scale` = 1.25. We train for 100 epochs with batch size 128 and seed 43. Mixed precision is not used; all runs fit on a single GPU.

Glucodensity view computation. The Glucodensity view used by X-CGM-JEPA compresses one daily CGM window into an image-like distributional summary that captures *joint* structure between glucose level, glucose velocity, and glucose acceleration, and is therefore complementary to the time-domain signal seen by f_θ . Given a daily CGM window $g_{1:288}$ we map indices to a continuous time axis $t = 5i/60$ in hours and fit a non-parametric smoothing spline $\tilde{g}(t)$ via `scipy.interpolate.UnivariateSpline` with smoothing factor 1.0. From this smoothed curve

we obtain three pointwise channels:

$$G(t) = \tilde{g}(t), \quad \dot{G}(t) = \frac{d\tilde{g}}{dt}, \quad \ddot{G}(t) = \frac{d^2\tilde{g}}{dt^2},$$

i.e., level, speed, and acceleration. We then compute three two-dimensional Gaussian kernel-density estimates for the channel *pairs* (G, \dot{G}) , (G, \ddot{G}) , and (\dot{G}, \ddot{G}) . Each KDE is evaluated on a 32×32 regular grid spanning the empirical 1st–99th percentile range of the corresponding channel pair (this trimming makes the grid robust to occasional spline-derivative spikes), and is normalized by its maximum density value to lie in $[0, 1]$. Stacking the three normalized KDE images along the channel axis gives a single 3-channel “Glucodensity image” $\mathbf{D} \in \mathbb{R}^{32 \times 32 \times 3}$ per window. Finally, we tile \mathbf{D} into non-overlapping spatial patches of size 8×8 in a Vision-Transformer-style layout, producing $4 \times 4 = 16$ patches that each carry all three channels jointly (i.e., each patch has shape $8 \times 8 \times 3$). Each patch is flattened into a 192-dimensional token, yielding a sequence of 16 tokens that is fed to the Glucodensity encoder g_ψ .

Pre-computation and caching. The KDE step is by far the most expensive part of the data pipeline: a fresh KDE evaluation per (window, pair, grid) tuple recomputes the same density tensor at every gradient step, dominating wall time even when the rest of the model is small. Because the Glucodensity view is a deterministic function of the daily CGM window (no augmentation, no stochasticity, no learnable parameters upstream), we instead precompute it once over the full pretraining corpus before training begins (see `utils/precompute_glucodensity.py`). The precompute job iterates over the same windowed dataset that pretraining uses, calls the procedure described above for every $(subject, split_idx)$ pair, and stores the resulting patches in a single keyed pickle cache together with the configuration (`gridsize = 32`, `spatial_patch_size = 8`, `patch_size = 12`, `series_split_size = 288`). At training time, the data loader looks up the cached Glucodensity patches by sample key, eliminating KDE evaluation from the training loop entirely; eight CPU workers (`gluco_kde_workers = 8`) are used only during precomputation. Precomputation runs once per dataset version on commodity CPU hardware and the resulting cache is checkpointed to disk and reused across all subsequent runs.

M.5.3. End-to-End Pipelines

For clarity, we summarize the full data flow at training time and at evaluation time. Both pipelines share the preprocessing stack of Section M.4.3.

Pretraining pipeline.

1. **Load** the pooled pretraining CSV (`cgm_initial_cohort.csv`, 22 Stanford + 206 Colas subjects, ≈ 389 k rows at 5-minute cadence).
2. **Slice** each subject’s stream into 24-hour windows of length 288.
3. **Tokenize** each window into $P=24$ non-overlapping hourly patches of size 12.
4. **(X-CGM-JEPA only)** Look up the precomputed Glucodensity tensor for the same window from the pickle cache (Section M.5.2); no live KDE.
5. **Mask** a random subset of patches at the configured mask ratio (default 0.25, varied in the ablation), splitting the window into context (visible) and target (masked) sets.
6. **Forward.** Context encoder f_θ encodes visible patches; EMA target encoder $f_{\bar{\theta}}$ encodes the full window and provides the target latents at masked positions; predictor p_ϕ predicts the target latents from the context. For X-CGM-JEPA, an auxiliary cross-view predictor q_ω predicts the masked Glucodensity embedding $\mathbf{u} = g_\psi(\mathbf{D}^{(t)})$ from the same context.

7. **Backward.** Total loss $\mathcal{L}_{\text{CGM}} + \lambda \mathcal{L}_{\text{GD}}$ (with $\mathcal{L}_{\text{GD}}=0$ for vanilla CGM-JEPA); Adam step on $\theta, \phi, \omega, \psi$; $\bar{\theta}$ is updated by EMA of θ at momentum 0.997. Gradients are stop-gradiented on the CGM target branch and *flow* into g_ψ .
8. **Checkpoint.** After 100 epochs, the encoder f_θ is logged as a versioned wandb artifact together with all metadata (mask ratio, λ , seed) so it is fully reproducible at downstream time.

Downstream pipeline (linear probe).

1. **Resolve** a pretrained encoder by its wandb artifact version. Architecture and tokenizer dimensions are read from the artifact metadata, so the loader can reconstruct the model without recourse to a separate checkpoint config file.
2. **Load** the labeled subject set from `train_split.json` (initial cohort, $n=27$) and `validation_split.json` (validation cohort, $n=17$); each subject’s daily window is already on the 5-minute grid via Section M.4.3.
3. **Freeze** f_θ ; route each labeled window through the same patchify \rightarrow encode pipeline used at pretraining time, then mean-pool the patch tokens to obtain a fixed-dimensional subject embedding $\mathbf{z} \in \mathbb{R}^d$ ($d=96$ for the encoders in this paper).
4. **Probe.** Fit an ℓ_2 -regularized logistic-regression probe (LogisticRegressionCV) with class-balanced weighting and inner 2-fold CV over the regularization grid $C \in \{10^{-3}, 10^{-2}, 10^{-1}, 1, 10, 100\}$, scored by AUROC. Outer 2-fold cross-validation is repeated for 20 random seeds, giving $20 \times 2 = 40$ paired test folds per (*encoder, task*) cell.
5. **Evaluate.** Report mean AUROC, PR-AUC, and F1 across folds and use a paired bootstrap test for headline comparisons. Optional probes (Linear SVC, Ridge, Random Forest, kNN) follow the same outer protocol.

The *evaluation pipeline* is parameterized by an (`extract_method, val_extract_method`) pair: *in-clinic venous* (`ctru_venous` \rightarrow `ctru_venous`) trains and tests on the OGTT venous trace; *cross-modality transfer* (`ctru_venous` \rightarrow `cgm_home_mean`) trains on venous and tests on CGM, evaluating modality robustness; *in-domain home CGM* (`cgm_home_mean` \rightarrow `cgm_home_mean`) restricts both training and testing to the at-home CGM mean.

M.5.4. Self-Supervised Learning Baselines

We compare CGM-JEPA and X-CGM-JEPA against two SSL baselines, each pretrained from scratch on the same pooled CGM corpus and evaluated under the identical linear-probe pipeline of the previous subsection. To control for capacity differences, we deliberately match the baseline encoder sizes to the size of our own context encoder; see the per-baseline notes below.

TS2Vec [30]. Pretraining objective. Hierarchical contrastive representation learning for time series, where positive pairs are obtained by random cropping of the same series and the contrastive loss is aggregated across multiple temporal scales via dilated convolutions.

Architecture. A stack of 10 dilated 1D-convolutional residual blocks (`depth = 10`) with hidden width 64 producing a representation of dimension 96 (matched to ours), no Transformer attention. Input is the raw univariate glucose stream (no patchification, no tokenization).

Pretraining hyperparameters. Learning rate 10^{-3} (Adam, default), batch size 128, maximum input length 3000 timesteps, `temporal_unit=0` (contrast at the finest temporal scale), 100 epochs.

Pipeline notes. TS2Vec’s reference implementation expects NaN to mark missing values, so we convert our -1 sentinels (Section M.4.3) to NaN on the fly. We also enable z-score normalization at the dataset-statistics step (`normalize_x=True` when computing the loader’s mean/std), following the original TS2Vec recipe; this is the only baseline where we deviate from the otherwise-default `normalize_x=False`, because the contrastive loss is sensitive to absolute-scale drift across subjects.

GluFormer [20]. Pretraining objective. Masked-token prediction over a discrete glucose vocabulary, analogous to BERT-style masked language modeling but on glucose tokens.

Tokenization. Continuous glucose values are quantized into $K=280$ uniformly spaced bins between the empirical min and max of the corpus, plus one extra index reserved for padding (vocabulary size $K+1=281$). The bin width is therefore $(g_{\max} - g_{\min})/280$ mg/dL.

Architecture (size-matched). We deliberately reduce GluFormer below the configuration in the original paper: token embedding dim 96, 6 attention heads, 3 encoder layers, feed-forward width 192 ($= 2 \times \text{embed dim}$), maximum sequence length 25,000 tokens (sufficient to cover the longest sliding windows produced under stride 144), dropout 0.0. The original GluFormer architecture is much wider/deeper and was developed for substantially larger CGM corpora; on our pooled corpus of ≈ 400 subject-days a full-size GluFormer would dominate the dataset and overfit, so we shrink it to match our own context encoder so that any SSL-vs-SSL difference reflects the *objective* rather than parameter-count.

Pretraining hyperparameters. Adam with learning rate 10^{-4} , exponential LR schedule (`step_size=100`, `gamma=0.99`) matching our CGM-JEPA run, gradient clipping at norm 1.0, batch size 128, 101 epochs, seed 43. The masking rate matches the value reported in the original paper (default: 25%); padded positions are excluded from the cross-entropy loss.

M.5.5. TSFM Baselines

For zero-shot probing of generic time-series foundation models (TSFMs), we compare against two off-the-shelf TSFMs without any glucose-specific pretraining or finetuning. In both cases we follow the standard inference recipes published by the original authors for downstream classification, restricted to the inputs we use elsewhere in this paper.

Mantis [10]. Checkpoint. `paris-noah/Mantis-8M`, the publicly released 8M-parameter Mantis8M model loaded via the official `mantis` Python package (`Mantis8M.from_pretrained(...)` wrapped in a `MantisTrainer`, exactly as in the project’s reference scripts).

Inference protocol. Mantis was trained on inputs of length 512, and the official `MantisTrainer.transform` API expects this length verbatim. Since our daily CGM window is 288 steps, we follow the standard practice from the released code base and *linearly interpolate* the window up to length 512 (`F.interpolate(..., mode="linear")`) before passing it to the encoder; the channel axis is set to 1 for univariate input, giving a final shape $(B, 1, 512)$. The model is run under `torch.no_grad()` and returns a single fixed-dimensional embedding per window, which we use directly as the downstream feature without any additional pooling.

MOMENT [12]. Checkpoints. We evaluate both released sizes, `AutonLab/MOMENT-1-small` and `AutonLab/MOMENT-1-large`, loaded through the official `momentfm` package as `MOMENTPipeline.from_pretrained`.

Inference protocol. We initialize each pipeline with the kwargs the MOMENT authors prescribe for *embedding-mode* usage in their classification tutorial.¹ concretely `model_kwargs={"task_name": "embedding", "n_channels": 1}`, followed by `model.init()` and `model.eval()`. MOMENT also expects an input length of 512; rather than interpolating, we follow MOMENT’s recommended approach for short series and *left-pad* our 288-step daily window with zeros to length 512 and pass an explicit `input_mask` (1 at real positions, 0 at padded positions) so the encoder ignores the synthetic prefix. The pipeline is called as `output = pipeline(x_enc=x, input_mask=input_mask)` under `torch.no_grad()` and we use `output.embeddings` directly as the downstream feature; no additional pooling is applied.

Common to both TSFMs. Both encoders are frozen at their published weights; no fine-tuning, prompt-tuning, or domain adaptation is performed. The TSFM-derived embeddings are fed to the same linear probe described in Section M.5.3, so the only difference between rows in the TSFM comparison is the upstream encoder. Any gap between TSFM rows and our CGM-JEPA / X-CGM-JEPA rows therefore isolates the value of CGM-specific pretraining rather than reflecting evaluation-pipeline asymmetries.

M.6. Societal Impact

Broader impacts. Type 2 Diabetes (T2D) affects over 537 million adults globally, making early detection a public-health priority. The two principal pathways toward T2D, insulin resistance and β -cell dysfunction, implicate different lifestyle and therapeutic responses, so distinguishing them, not merely flagging overall risk, is what makes early intervention actionable. Yet the gold-standard test for these subphenotypes, the venous oral glucose tolerance test, is invasive and resource-intensive, ruling it out for population-scale screening. By showing that self-supervised representations from unlabeled CGM data support clinically meaningful subphenotype discrimination under realistic deployment conditions, our work contributes a foundation for non-invasive, scalable metabolic risk stratification using consumer-grade wearables, lowering the barrier to targeted early prevention.

Limitations and Ethical Considerations. While population-scale CGM-based screening holds great promise for early metabolic risk stratification, it must be guided by careful attention to safety, fairness, and privacy. The possibility of misuse by malicious actors underscores the importance of responsible development. Although we advocate for open science and release code, training configurations, and pretrained weights, health data requires a delicate balance between reproducibility and participant confidentiality: we release de-identified CGM only from participants who consented to data sharing, while the full clinical cohorts remain access-controlled.

Importantly, CGM-JEPA’s family is a research prototype and is not intended for clinical use. It has not been validated as a diagnostic tool and should not be used for medical decision-making without formal regulatory approval. While our subgroup analysis (Section 2.6) shows the cross-view objective compresses worst-to-best AUROC gaps across demographic strata, per-subgroup sample sizes are small ($n = 5\text{--}12$) and these patterns are not yet validated beyond our cohorts; deployment without re-evaluation could produce inequitable outcomes our analysis does not predict. Clinical deployment would require prospective multi-site validation and compliance with the relevant medical-device regulatory framework.

Finally, while CGM-JEPA’s family methodology is designed to be generalizable, our evaluation is

¹moment-timeseries-foundation-model/moment-tutorials/classification.ipynb

limited to two cohorts ($N=27$ and $N=17$ in the public-release subset), one CGM device, and OGTT-derived labels for two subphenotypes. Further research is needed across broader device ecosystems, longer temporal windows, additional metabolic outcomes, and more diverse populations.